RESEARCH ARTICLE
SOLID EARTH: SEISMOLOGY

Earth and Planetary Physics
10: 1053–1060, 2026
doi: 10.26464/epp2026092

Seismic evidence linking dehydration to the low-velocity layer above the 410 km discontinuity

QiuYue Jin, and XiaoBo He*

Marine Science and Technology College, Zhejiang Ocean University, Zhoushan Zhejiang 316022, China

Key Points:

- Dehydration melting is attributed to low-velocity layer formation atop 410 km.
- P410s amplitude variations are controlled by water content at 410 km.
- Pacific slab subduction constrains deep water circulation in NE China.

Citation: Jin, Q. Y., and He, X. B. (2026). Seismic evidence linking dehydration to the low-velocity layer above the 410 km discontinuity. *Earth Planet. Phys.*, *10*(6), 1053–1060. http://doi.org/10.26464/epp2026092

Abstract: The low-velocity layer above the 410 km discontinuity is widely attributed to dehydration-induced melting in the upper mantle; however, direct seismic evidence for this linkage remains scarce. Situated at the leading edge of the Northwest Pacific subduction zone, northeast China provides an exceptional natural laboratory owing to the deep subduction and stagnation of the Pacific slab. Using teleseismic waveform data from 327 broadband stations, we extracted 40,236 high-quality P-wave receiver functions, applied common conversion point (CCP) stacking along the 42°N profile (115°E–130°E) to image mantle discontinuities, and probed the origin of the low-velocity layer. Our results revealed pronounced lateral heterogeneity: regions with a well-developed low-velocity layer exhibited sharp and strong P410s phases, whereas adjacent regions lacking such a layer showed markedly weakened or absent signals. Forward modeling demonstrates that the transitional thickness of the 410 km discontinuity, which is closely governed by water content, exerts first-order control on P410s amplitudes, with broader discontinuities progressively diminishing converted-wave energy and weak-P410s regions yielding an average P410s/P660s amplitude ratio of 0.46 ± 0.07. Modeling based on the IASP91 velocity structure suggests an ~11 ± 3 km gradient layer at the 410 km discontinuity. These spatial correlations provide direct seismic evidence that dehydration at the 410 km discontinuity sharpens the phase boundary and enhances the converted phases, whereas persistent hydration broadens the transition zone and weakens the P410s signals. This study offers new constraints on deep-water circulation, mantle material transport, and the role of Pacific slab subduction beneath the East Asian continental margin.

Keywords: 410 km discontinuity; low-velocity layer; dehydration melting; P-wave receiver functions; pacific slab subduction

1. Introduction

The mantle transition zone (MTZ) plays a pivotal role in the deep-water cycle of the Earth, with the 410 km discontinuity marking a key boundary where hydration and dehydration processes strongly influence seismic properties (e.g., Bercovici and Karato, 2003; Karato et al., 2006). A low-velocity layer (LVL) immediately above this discontinuity has often been attributed to dehydration-induced melting (e.g., Hier-Majumder and Courtier, 2011; Fomin and Schiffer, 2019; Han GJ et al., 2021; Sun YZ et al., 2021; Li GH et al., 2022, 2025; Chen J et al., 2026); however, whether this feature truly originates from water release at 410 km remains uncertain. This question arises in light of Green et al. (2010), who argued that the subducting lithosphere carries negligible water below 400 km depth and proposed that continental lithosphere delamination may govern deep-water cycling. Other models also contend that the MTZ contains little water (Houser, 2016), with a dry MTZ inferred from the electrical conductivities of wadsleyite and ringwoodite (Yoshino et al., 2008) and geomagnetic diurnal variations (Zhang HQ et al., 2022). Resolving this debate requires direct seismic evidence linking the low-velocity layer above the 410 km discontinuity to slab dehydration-driven partial melting at that depth. Establishing such a connection is the starting point of this study.

Northeast (NE) China provides an exceptional natural laboratory to investigate this problem. The Pacific slab has subducted to great depths and stagnated in the MTZ (e.g., Li J et al., 2008, 2013; Zhao DP et al., 2009; Ye LL et al., 2011; Lu MW et al., 2020; He XB et al., 2025), creating conditions favorable for testing the relationship between slab-derived water release, mantle melting, and seismic discontinuity sharpness. Previous studies have reported heterogeneous seismic signals in this region (e.g., Ai YS et al., 2007; Huang R et al., 2014; Guan Z and Niu FL, 2017; Han GJ et al., 2021; Yang F et al., 2021; Tang Z et al., 2023; Zhu S et al., 2026), but the physical mechanism controlling the amplitude and character of converted

First author: Q. Y. Jin, jinqiuyue@zjou.edu.cn
Correspondence to: X. B. He, xiaobo.he@zjou.edu.cn
Received 19 AUG 2026; Accepted 24 SEP 2026.
First Published online 04 NOV 2026.
©2026 by Earth and Planetary Physics.

phases remains poorly constrained.

In this study, we employed a dense broadband seismic array and high-resolution receiver function imaging to probe mantle discontinuities beneath NE China (Figure 1). By focusing on the transitional thickness and amplitude variations of the 410 km discontinuity, we aimed to resolve whether dehydration processes directly sharpen the phase boundary and generate the low-velocity layer. This approach addresses the fundamental question of how slab-derived water influences the seismic expression of the 410 km discontinuity and the formation of the low-velocity layer atop the MTZ.

2. Data and Analysis

We used teleseismic three-component waveform data recorded by 327 broadband seismic stations in NE China and adjacent regions, including 200 permanent stations from the China Seismic Network and 127 temporary stations from the NECESSArray (Figure 1). Events with moment magnitudes $M_w \geq 5.5$ and epicentral distances between 30° and 90° were selected to ensure clear teleseismic P-wave arrivals and reliable receiver-function estimates. After event selection, 4576 earthquakes were retained for subsequent processing.

The raw SAC waveforms were pre-processed by removing the mean and linear trends, applying a taper, resampling to 0.025 s, and bandpass filtering between 0.05 and 1.0 Hz. For each event-station pair, a 130-s time window was extracted from 10 s before to 120 s after the theoretical P-wave arrival. The horizontal components were then rotated into the radial and transverse directions based on the back azimuth of the event.

The P-wave receiver functions were computed using the frequency-domain water-level deconvolution of the radial component by the vertical component. A water level of 0.01 and Gaussian factor of 1.0 were adopted. Receiver functions with high signal-to-noise ratios were carefully selected. For each station, an individual receiver function was rejected if its maximum absolute amplitude within the pre-P window (10–2 s before the direct P-wave arrival) exceeded that of the station-averaged receiver function in the same window. After quality control, 40,236 high-quality P-wave receiver functions were retained for common conversion point (CCP) imaging. Seispy, a Python module for batch calculation and post-processing of receiver functions (Xu MJ and He J, 2022), was employed for receiver-function computation and CCP stacking.

3. Results and Discussion

3.1 CCP Stacking of Receiver Functions

CCP stacking was performed along an east–west profile at 42°N between 115°E and 130°E. The IASP91 model (Kennett and Engdahl, 1991) was used as the reference velocity model for ray tracing and time-to-depth conversion. Receiver functions were

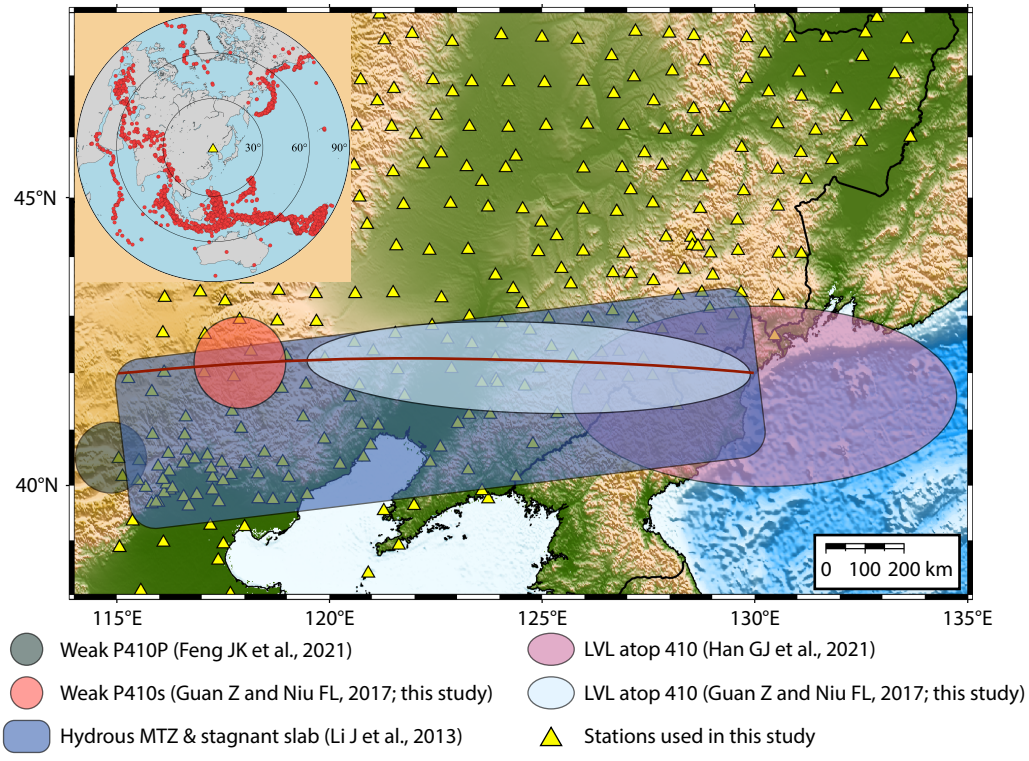

Figure 1. Distribution of seismic stations and previous results in the study area. Yellow triangles denote seismic stations; the inset in the upper left shows one station and the distribution of recorded earthquakes (red solid circles). Previous studies are also indicated: weak P410P inferred from ambient noise interferometry extracting body-wave reflections (Feng JK et al., 2021) and weak P410s inferred from receiver function studies (Guan Z and Niu FL, 2017), with their study regions marked by filled circles; hydrous MTZ and stagnant slab based on triplication waveform modeling (Li J et al., 2013), shown as filled rectangles; and detection of the low-velocity layer (LVL) above 410 km (Guan Z and Niu FL, 2017; Han GJ et al., 2021), represented by filled ellipses. The present study focuses on the 42°N profile, indicated by the red solid line.

migrated to depths of 0–800 km with a depth interval of 1 km. Circular CCP bins with a radius of approximately 1° were used to gather the receiver functions, and the profile was sampled at an interval of 11 km. The CCP stacking results of the receiver functions along the 42°N profile are presented in Figure 2, along with the results from Guan Z and Niu FL (2017) for comparison. Overall, our results consistently revealed the same major features as those reported by Guan Z and Niu FL (2017). However, the signals in this study appear to be slightly different from those of Guan Z and Niu FL (2017). This difference may reflect variations in data coverage, imaging methodology, and figure presentation rather than fundamental discrepancies in the underlying structure. Importantly, our analysis focuses on the lateral variations in the relative amplitudes rather than their absolute values; therefore, such amplitude differences do not affect our interpretation. In addition, we employed the IASP91 one-dimensional (1-D) velocity model for the time-to-depth conversion, whereas Guan Z and Niu FL (2017) used a regional velocity model. Because our analysis focused more on lateral variations and the P410s/P660s amplitude ratio rather than absolute depths, the choice of velocity model did not significantly affect our conclusions. Regional models vary considerably, making it difficult to select one fairly. Therefore, we prefer to use a global 1-D model to ensure consistency and comparability.

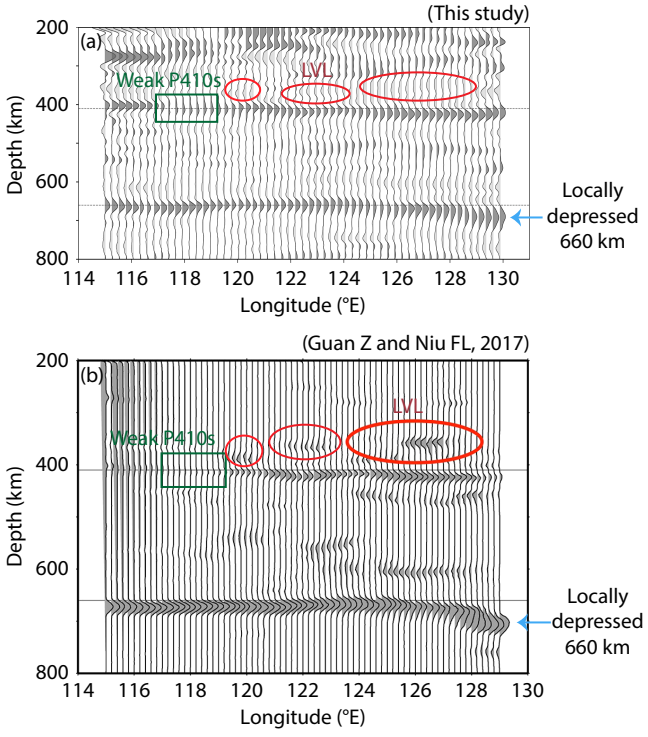

Figure 2. Common conversion point (CCP) stacking results along the 42°N profile. (a) Results from this study. (b) Results from Guan Z and Niu FL (2017) for comparison. The red ellipses highlight the low-velocity layer (LVL) above the 410-km discontinuity, and the green rectangles mark regions of weak P410s signals. Both our results and those of Guan Z and Niu FL (2017) consistently reveal weak P410s amplitudes and widespread LVL development above 410 km.

The most striking observations are as follows. Along this transect, the P660s signal shows little lateral variation and consistently appears as a clear, prominent phase, with the only anomaly being a markedly delayed P660s in the easternmost segment, indicating a locally depressed 660 km discontinuity. In contrast, the P410s signal exhibits pronounced lateral variability. In the western segment (117°E–119°E), P410s is extremely weak, whereas it becomes more distinct farther east. Moreover, an additional polarity-reversed signal is observed above the clear P410s phases in the eastern region, indicating the presence of a LVL above the 410 km discontinuity. No such LVL signal was detected in the 117°E –119°E segment. Previous studies attributed this LVL to melts generated by dehydration (Han GJ et al., 2021). In the southwestern part of the weak-P410s region (Figure 1), Feng JK et al. (2021) reported weak P410P signals extracted via ambient noise interferometry as body-wave reflections from the 410 km discontinuity.

To illustrate the lateral variations in the CCP stacking results better, we performed a fourth-root vespagram analysis of the receiver functions along the 42°N profile. Two longitudes were selected along the transect: 118°E and 126°E. As shown in Figure 3, the results clearly demonstrate that weak P410s signals occur in

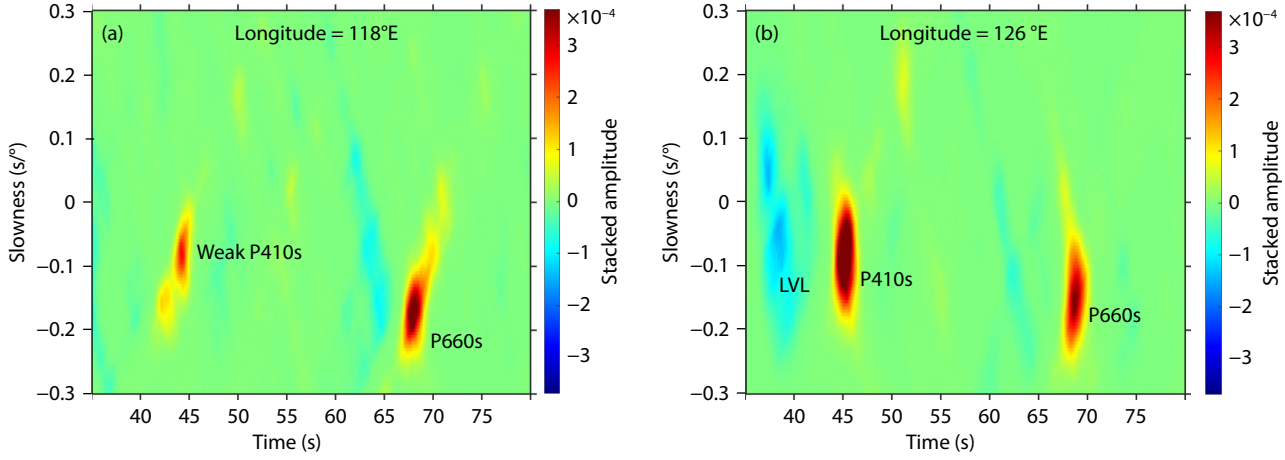

Figure 3. Fourth-root vespagram analysis of receiver functions along the 42°N profile. (a) Longitude 118°E and (b) longitude 126°E. The results highlight the presence of weak P410s signals in the western segment, whereas the eastern segment exhibits prominent P410s. In addition, an LVL is detected above the 410 km discontinuity.

the western segment at 118°E, whereas prominent P410s signals are observed in the eastern segment at 126°E. In addition, a LVL was detected above the 410 km discontinuity at 126°E; however, no such LVL was observed at 118°E where weak P410s occurred.

3.2 Thickness of the 410 km Discontinuity as the Primary Control on P410s Amplitudes

To investigate the factors responsible for weak P410s signals, we conducted synthetic receiver-function calculations to examine how variations in the transitional thickness at the 410 km discontinuity influenced P410s amplitudes, as illustrated in Figure 4. The theoretical results clearly show that increasing the thickness leads to a pronounced reduction in the P410s amplitude. Once the thickness exceeds approximately 20 km, the P410s signal becomes extremely weak such that it is nearly unobservable.

These findings demonstrate that transitional thickness exerts a dominant control on P410s amplitudes. In other words, the first-order factor governing the P410s strength is the width of the phase transition at 410 km, whereas other influences, such as compositional variations, play a secondary role.

3.3 Estimation of Transitional Thickness of 410 km Discontinuity

As shown in Figure 5, we constrained the transitional thickness of the 410 km discontinuity in regions with weak P410s signals using the P410s/P660s amplitude ratio. Our analysis focused on the longitude segment from 117°E–119°E, where CCP stacking was applied to obtain the receiver functions. For each longitude within this range, we calculated the P410s/P660s amplitude ratio from the stacked receiver functions and averaged the seven values across the segment to derive a representative ratio. Amplitudes were measured using a peak-to-zero rather than peak-to-peak approach, as receiver functions are dominated by pulse-like signals, and the peak-to-zero approach provides a more stable metric. We recognize that the amplitudes may be affected by factors such as source radiation patterns, focusing/defocusing effects, and heterogeneous structures. Although these influences cannot be fully eliminated, our averaging strategy, the use of CCP stacking, and reliance on the P410s/P660s ratio help to mitigate random variations and enhance the robustness of the amplitude measurements.

Our workflow to constrain the thickness of 410 km discontinuity is as follows. We first derived the observed P410s/P660s amplitude ratio from the CCP stacking results and then constructed a series of synthetic models to fit this ratio. In these models, the velocity structure at 660 km is taken directly from the IASP91 model, whereas the 410 km structure is based on IASP91 but modified by introducing a transitional thickness. By systematically varying the thickness of the 410 km discontinuity, we determined the values that best reproduced the observed ratios across the profile. Our approach involved iteratively varying the transitional thickness to match the observed amplitude ratios; through this trial-and-error procedure, we obtained the final estimate of 0.46 ± 0.07 corresponding to a transitional thickness of 11 ± 3 km, demonstrating that the 410 km discontinuity is broadened rather than sharp.

Mineral physics experiments provide strong evidence that such transitional discontinuities are associated with hydration because the presence of water increases the width of the phase transition (Smyth and Frost, 2002). The estimated thickness of 11 km is noticeably greater than the ~7 km thickness expected for an anhydrous 410 km discontinuity in subduction zones (Katsura et al., 2004). Similarly, Vinnik et al. (2020) reported widths ranging from 10–22 km in the eastern Yangtze Craton using P-wave receiver functions, consistently exceeding the 7-km value predicted under dry conditions, which agrees with our findings.

In this analysis, we considered only the effect of hydration on the P410s amplitudes, specifically its control on the transitional thickness of the 410 km discontinuity. We argue that this thickness exerts a first-order influence on amplitude variations, whereas compositional effects are likely secondary. Although the use of the P410s/P660s amplitude ratio reduced the impact of source radiation patterns, our results relied on the IASP91 velocity model (Kennett and Engdahl, 1991). Previous studies suggest that basaltic enrichment may occur near the 660-km discontinuity (e.g., Feng JK et al., 2021; Zhou BX and He XB, 2024). If basalt enrichment were also present in our study area, it would reduce the velocity contrast at 660 km and lower the P660s amplitudes (Zhang M et al., 2019). In this case, explaining the observed low P410s/P660s ratio would require an even greater reduction in the P410s amplitude, implying a thicker 410 km transitional layer. Thus, our estimate of 11 km may represent a lower bound, and the actual thickness may be larger. Future seismic investigations that better constrain the velocity structure near 660 km will provide more accurate compositional constraints on MTZ discontinuities. Unfortunately, we were unable to quantitatively constrain water content from the estimated transitional thickness of 410 km. Establishing such a constraint requires a quantitative mineralogical relationship between discontinuity thickness and hydration, which is currently lacking.

3.4 Temporal Evolution of MTZ Hydration and Dehydration Melting

To explain our seismic observations, we proposed a time-evolving model of MTZ hydration and dehydration melting, as illustrated in Figure 6. Before the arrival of the subducting slabs in the MTZ, when slab-derived hydration has not yet occurred, the transition zone remains essentially anhydrous. Under these conditions, the 410 km discontinuity is sharp.

Once slab subduction and dehydration begin, the MTZ undergoes progressive hydration. This process broadens the phase transition at 410 km, transforming the discontinuity into a transitional boundary. With continued slab dehydration, the hydration of the MTZ increases until saturation is reached. At this stage, dehydration triggers partial melting, producing the LVL observed above the 410 km discontinuity. Following dehydration, the discontinuity reverts from transitional to sharp.

In contrast, the western regions exhibited insufficient hydration and never reached saturation. Consequently, dehydration and melting did not occur and no LVL developed above 410 km. Here, the discontinuity remained transitional, leading to reduced P410s

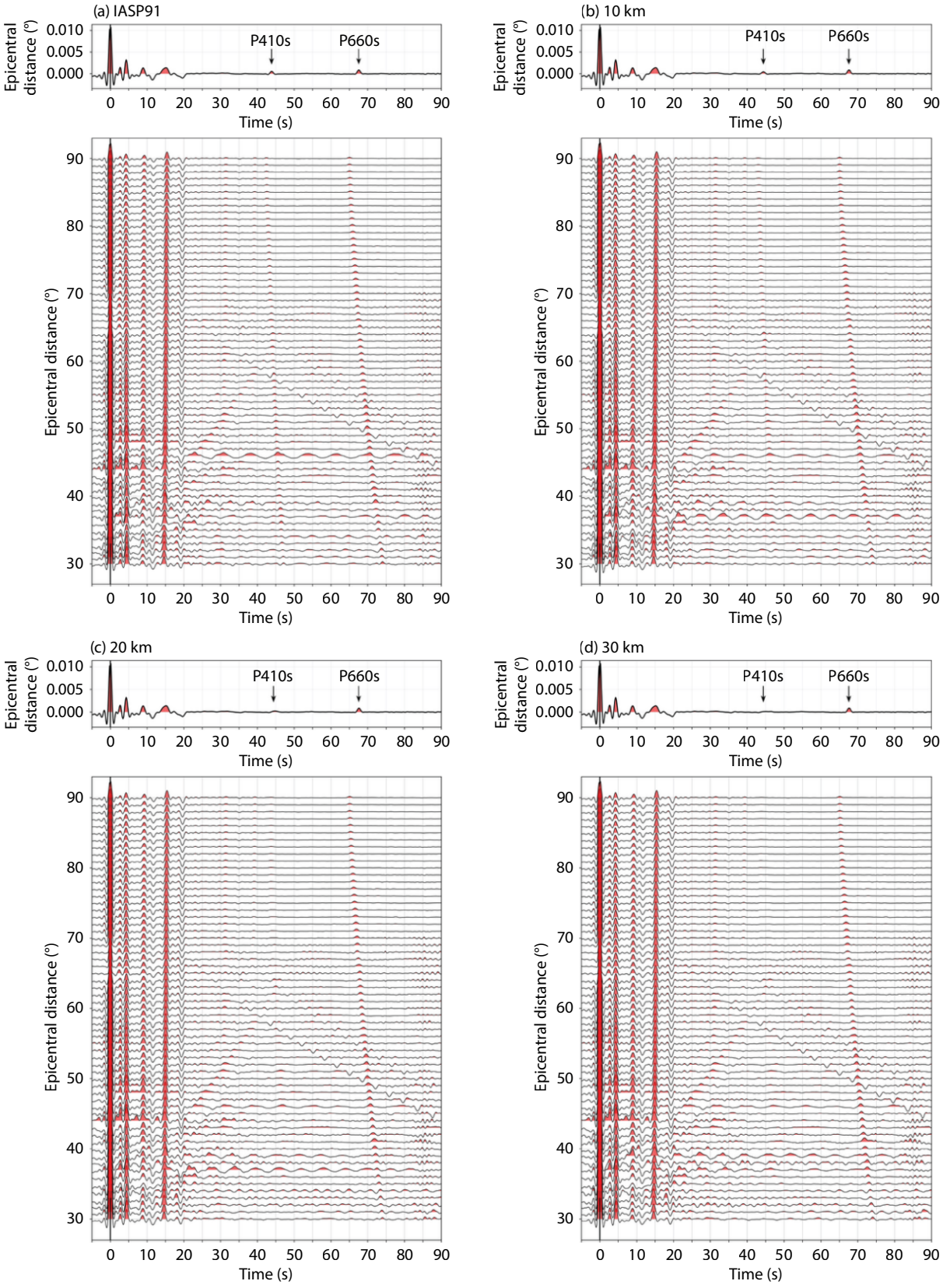

Figure 4. Synthetic receiver-function calculations illustrating the effect of transitional thickness at the 410 km discontinuity on P410s amplitudes. (a) IASP91 velocity model with a sharp 410 km discontinuity. (b) Transitional thickness of 10 km. (c) Transitional thickness of 20 km. (d) Transitional thickness of 30 km.

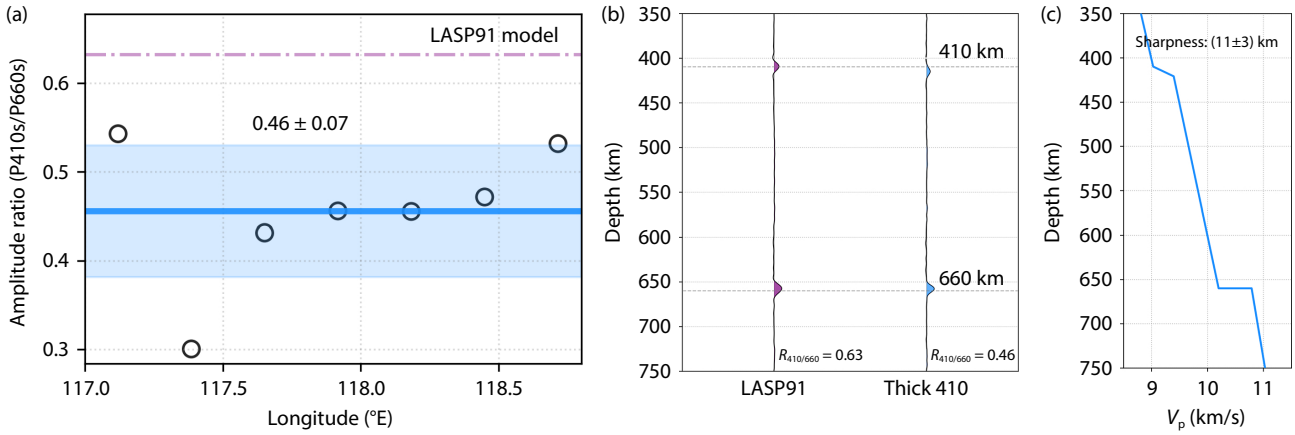

Figure 5. Estimation of the transitional thickness of the 410 km discontinuity in regions with weak P410s signals. (a) Amplitude ratio of P410s/P660s, with the observed value of 0.46 significantly lower than the IASP91 model ratio of 0.63. (b) Comparison of receiver-function waveforms between observations and the IASP91 model. (c) Derived thickness 11 km of the 410 km discontinuity and the corresponding one-dimensional velocity model, with depths other than 410 km taken from the IASP91 model. $R_{410/660}$ is amplitude ratio of P410s/P660s and V_p is P-wave velocity.

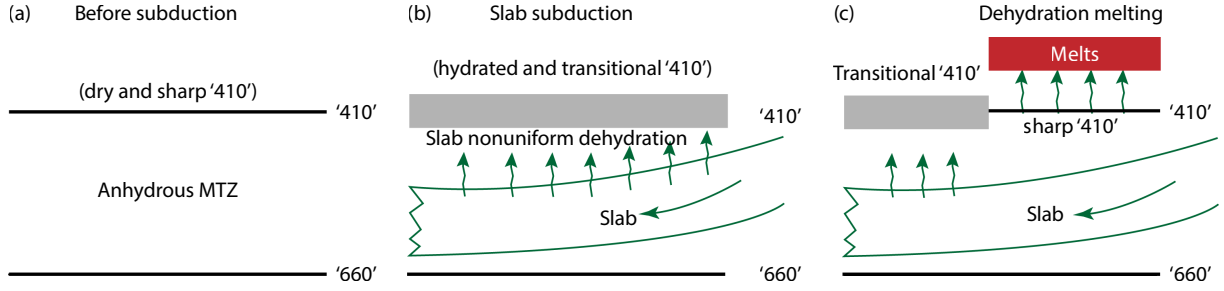

Figure 6. Conceptual model to explain temporal evolution of mantle transition zone (MTZ) hydration and dehydration melting. (a) Before slab subduction: anhydrous MTZ with a sharp 410 km discontinuity. (b) Slab subduction and dehydration: hydration broadens the phase transition, producing a transitional 410 km discontinuity. (c) Continued slab dehydration: saturation triggers dehydration melting and a low-velocity layer above 410 km, whereas western regions remain transitional due to insufficient hydration.

amplitudes—consistent with our observations of weak P410s signals.

When combined, the lateral variations in the P410s amplitude and presence or absence of the LVL above 410 km reflect the evolutionary sequence of the MTZ, from anhydrous to hydrated, and ultimately to dehydration-induced melting. However, this temporal evolution model is speculative and should be regarded as a conceptual framework. Its validity requires further testing through geodynamic simulations and mineral physics experiments. Nevertheless, the model highlights the scientific novelty of our study by linking present-day spatial variations to a possible evolutionary sequence of mantle hydration and dehydration melting.

3.5 Stishovite and Al-bearing Stishovite as Deep-mantle Water Carriers

Recent studies have emphasized the role of silica polymorphs, particularly stishovite, as potential carriers of water into the deep mantle. Two complementary lines of work have provided contrasting insights into the water storage capacity of stishovite under extreme conditions.

Wang F et al. (2026) focused on pure stishovite without the influence of additional elements. High-pressure experiments have demonstrated that stishovite exhibits significant water solubility only at relatively low temperatures, even lower than the characteristics of cold subduction zones. However, at higher temperatures typical of the deep Earth, its water solubility decreases sharply and becomes negligible. These findings suggest that pure stishovite cannot effectively transport water into the deep mantle, clarifying its limited role in deep-Earth water cycling and indicating that earlier reports of high-water solubility may reflect either related phases or experimental artifacts.

In contrast, Liu D et al. (2026) examined Al-bearing stishovite and its denser polymorph, post-stishovite. Laboratory experiments revealed that both phases could incorporate approximately 2 wt% of water under deep mantle pressures and temperatures, with water storage capacity positively correlated with Al_2O_3 content. Importantly, variations in Al_2O_3 and H_2O concentrations influence the depth of the stishovite–post-stishovite transition, potentially explaining the occurrence of seismic scatterers across a broad depth range in the mid-mantle. This highlights the role of chemical heterogeneity in subducted lithologies in shaping the complex seismic structures observed in the interior of the Earth.

Taken together, these studies indicate that, although the role of pure stishovite in deep-water recycling is strongly limited by temperature effects, Al-bearing stishovite appears to be increasingly effective in storing water under higher pressures and temperatures. Thus, Al-bearing stishovite can be regarded as a plausible and potentially important mineralogical carrier for transporting water into the deep mantle, although its relative significance, compared with other mantle minerals, remains subject to ongoing investigation.

3.6 Alternative Pathways of Deep-water Transport

The MTZ can be hydrated either through the subduction of hydrous plates or by hydrous mantle upwelling, potentially rooted at the base of the mantle in the form of plumes (Bercovici and Karato, 2003). However, a key question is whether other mechanisms of water transport are equally or even more significant. Building on our previous studies, we highlighted two additional processes that should be considered as important pathways for recycling water back into the mantle.

The first involves subducting passive margins containing crustal (ultra)mafic intrusions that can deliver substantial water flux into the mantle (Pan CC and He XB, 2023). The second is the subduction of water-rich seamounts (He XB et al., 2022, 2025). Notably, Chesley et al. (2021) suggested that a subducting seamount may transport 3.2–4.7 times more water into the deep mantle than normal, unfaulted oceanic lithosphere.

The principal mineral phases capable of transporting water into the deep mantle are high-pressure polymorphs of silica, particularly stishovite. Both subducting continental margins and seamounts contain higher concentrations of silica than the typical oceanic crust. Consequently, they are two highly plausible carriers for water delivery to the deep mantle.

4. Conclusions

Our seismic imaging across NE China provides direct evidence that dehydration at the 410 km discontinuity sharpens the phase boundary and enhances the converted phases. Regions with a well-developed low-velocity layer exhibit strong P410s signals, whereas the water-bearing 410 km discontinuity lacking dehydration shows a broadened transition and weakened amplitudes. Forward modeling confirmed that the thickness of the 410 km gradient layer, governed by water content, exerts first-order control on P410s amplitudes. These findings establish a robust link between mantle hydration state and seismic discontinuity sharpness, offering new constraints on deep-water circulation, mantle material transport, and the role of Pacific slab subduction beneath the East Asian continental margin.

Acknowledgments

Figures were prepared using Generic Mapping Tools (Wessel and Smith, 1991). We are grateful to two anonymous reviewers and the editor for their insightful comments, which helped us improve the manuscript. The authors acknowledge the support from the Deep Earth Probe and Mineral Resources Exploration–National Science and Technology Major Project 2025ZD1005100 and the National Natural Science Foundation of China (Grant No. 42276049).

References

Ai, Y. S., Chen, Q. F., Zeng, F., Hong, X., and Ye, W. Y. (2007). The crust and upper mantle structure beneath southeastern China. *Earth Planet. Sci. Lett.*, *260*(3–4), 549–563. https://doi.org/10.1016/j.epsl.2007.06.009

Bercovici, D., and Karato, S. I. (2003). Whole-mantle convection and the transition-zone water filter. *Nature*, *425*(6953), 39–44. https://doi.org/10.1038/nature01918

Chen, J., Yu, H. Y., Fu, S. Y., Xu, F., Zhang, B. H., and Fei, H. Z. (2026). High melt fraction induced by the dehydration melting near the 410-km discontinuity. *Geophys. Res. Lett.*, *53*(16), e2025GL121527. https://doi.org/10.1029/2025gl121527

Chesley, C., Naif, S., Key, K., and Bassett, D. (2021). Fluid-rich subducting topography generates anomalous forearc porosity. *Nature*, *595*(7866), 255–260. https://doi.org/10.1038/s41586-021-03619-8

Feng, J. K., Yao, H. J., Wang, Y., Poli, P., and Mao, Z. (2021). Segregated oceanic crust trapped at the bottom mantle transition zone revealed from ambient noise interferometry. *Nat. Commun.*, *12*(1), 2531. https://doi.org/10.1038/s41467-021-22853-2

Fomin, I., and Schiffer, C. (2019). Water, hydrous melting, and teleseismic signature of the mantle transition zone. *Geosciences*, *9*(12), 505. https://doi.org/10.3390/geosciences9120505

Green, H. W. II, Chen, W. P., and Brudzinski, M. R. (2010). Seismic evidence of negligible water carried below 400-km depth in subducting lithosphere. *Nature*, *467*(7317), 828–831. https://doi.org/10.1038/nature09401

Guan, Z., and Niu, F. L. (2017). An investigation on slowness-weighted CCP stacking and its application to receiver function imaging. *Geophys. Res. Lett.*, *44*(12), 6030–6038. https://doi.org/10.1002/2017gl073755

Han, G. J., Li, J., Guo, G. R., Mooney, W. D., Karato, S. I., and Yuen, D. A. (2021). Pervasive low-velocity layer atop the 410-km discontinuity beneath the northwest Pacific subduction zone: Implications for rheology and geodynamics. *Earth Planet. Sci. Lett.*, *554*, 116642. https://doi.org/10.1016/j.epsl.2020.116642

He, X. B., Tao, J. T., Cao, Y., Pan, F. B., He, E. Y., Cao, L. M., and Zheng, Y. X. (2022). No seamount subduction, no magmatic arc? *Earth Planet. Phys.*, *6*(4), 424–429. https://doi.org/10.26464/epp2022031

He, X. B., He, M. L., Li, Y. B., Hu, J. S., Pan, F. B., Wang, Z. S., and Lei, J. S. (2025). Changbaishan volcanism: Is seamount subduction the missing piece? *J. Earth Sci.*, *36*(5), 2337–2340. https://doi.org/10.1007/s12583-025-0181-x

Hier-Majumder, S., and Courtier, A. (2011). Seismic signature of small melt fraction atop the transition zone. *Earth Planet. Sci. Lett.*, *308*(3-4), 334–342. https://doi.org/10.1016/j.epsl.2011.05.055

Houser, C. (2016). Global seismic data reveal little water in the mantle transition zone. *Earth Planet. Sci. Lett.*, *448*, 94–101. https://doi.org/10.1016/j.epsl.2016.04.018

Huang, R., Xu, Y. X., Luo, Y. H., and Jiang, X. H. (2014). Mantle transition zone structure beneath southeastern China and its implications for stagnant slab and water transportation in the mantle. *Pure Appl. Geophys.*, *171*(9), 2129–2136. https://doi.org/10.1007/s00024-014-0837-4

Karato, S. I., Bercovici, D., Leahy, G., Richard, G., and Jing, Z. C. (2006). The transition-zone water filter model for global material circulation: Where do we stand? In S. D. Jacobsen, et al. (Eds.), *Earth's Deep Water Cycle* (pp. 289–313). Washington, DC: American Geophysical Union. https://doi.org/10.1029/168gm22

Katsura, T., Yamada, H., Nishikawa, O., Song, M. S., Kubo, A., Shinmei, T., Yokoshi, S., Aizawa, Y., Yoshino, T., … Funakoshi, K. (2004). Olivine-wadsleyite transition in the system $(Mg, Fe)_2SiO_4$. *J. Geophys. Res.: Solid Earth*, *109*(B2), B02209. https://doi.org/10.1029/2003JB002438

Kennett, B. L. N., and Engdahl, E. R. (1991). Traveltimes for global earthquake location and phase identification. *Geophys. J. Int.*, *105*(2), 429–465. https://doi.org/10.1111/j.1365-246X.1991.tb06724.x

Li, G. H., Gao, Y., Zhou, Y. Z., Ju, C. H., Shi, Y. T., and Cui, Q. H. (2022). A low-velocity layer atop the mantle transition zone beneath the western Central Asian Orogenic Belt: Upper mantle melting induced by ancient slab

subduction. *Earth Planet. Sci. Lett.*, *578*, 117287. https://doi.org/10.1016/j.epsl.2021.117287

Li, G. H., Zhou, Y. Z., Bai, L., and Gao, Y. (2025). Low-velocity layer atop mantle transition zone and its dynamic effects in Chinese mainland and adjacent regions. *Rev. Geophys. Planet. Phys.* (in Chinese), *56*(5), 554–562. https://doi.org/10.19975/j.dqyxx.2024-062

Li, J., Chen, Q. F., Vanacore, E., and Niu, F. L. (2008). Topography of the 660-km discontinuity beneath northeast China: Implications for a retrograde motion of the subducting Pacific slab. *Geophys. Res. Lett.*, *35*(1), L01302. https://doi.org/10.1029/2007gl031658

Li, J., Wang, X., Wang, X. J., and Yuen, D. A. (2013). P and SH velocity structure in the upper mantle beneath Northeast China: Evidence for a stagnant slab in hydrous mantle transition zone. *Earth Planet. Sci. Lett.*, *367*, 71–81. https://doi.org/10.1016/j.epsl.2013.02.026

Liu, D., Yang, Y. N., Fei, H. Z., Wang, F., Purevjav, N., Ye, Y., Ishii, T., and Katsura, T. (2026). A systematic study of the pressure and temperature dependences of H_2O and Al_2O_3 solubility in Al-bearing stishovite and post-stishovite. *J. Geophys. Res.: Solid Earth*, *131*(8), e2025JB033119. https://doi.org/10.1029/2025jb033119

Lu, M. W., Lei, J. S., Zhao, D. P., Ai, Y. S., Xu, X. W., and Zhang, G. B. (2020). SKS splitting measurements in NE China: New insights into the Wudalianchi intraplate volcanism and mantle dynamics. *J. Geophys. Res.: Solid Earth*, *125*(3), e2019JB018575. https://doi.org/10.1029/2019jb018575

Pan, C. C., and He, X. B. (2023). Subducting passive continental margins with crustal (ultra)mafic intrusions: An underappreciated mechanism for recycling water back into the mantle. *Earth Planet. Phys.*, *7*(5), 576–581. https://doi.org/10.26464/epp2023074

Smyth, J. R., and Frost, D. J. (2002). The effect of water on the 410-km discontinuity: An experimental study. *Geophys. Res. Lett.*, *29*(10), 123-1–123-4. https://doi.org/10.1029/2001gl014418

Sun, Y. Z., Hier-Majumder, S., Tauzin, B., Walter, M., Ballmer, M., Xu, Y. G., and Kim, S. (2021). Evidence of volatile-induced melting in the northeast Asian upper mantle. *J. Geophys. Res.: Solid Earth*, *126*(10), e2021JB022167. https://doi.org/10.1029/2021jb022167

Tang, Z., Julià, J., Mooney, W. D., Mai, P. M., Yu, H. Z., and Wu, Y. Q. (2023). Seismic image of the mantle transition zone beneath northeastern China: evidence for stagnant Pacific subducting slab, lithospheric delamination and mantle upwelling. *Geophys. J. Int.*, *235*(2), 1872–1887. https://doi.org/10.1093/gji/ggad335

Vinnik, L., Deng, Y. F., Kosarev, G., Oreshin, S., Zhang, Z., and Makeyeva, L. (2020). Sharpness of the 410-km discontinuity from the P410s and P2p410s seismic phases. *Geophys. J. Int.*, *220*(2), 1208–1214. https://doi.org/10.1093/gji/ggz507

Wang, F., Chanyshev, A., Man, L. J., Song, Y. K., Wang, L., Ishii, T., Tsujino, N., Bhat, S., Farla, R., and Katsura, T. (2026). Limits of water storage in stishovite at deep mantle conditions. *Geophys. Res. Lett.*, *53*(13), e2025GL120078. https://doi.org/10.1029/2025gl120078

Wessel, P., and Smith, W. H. F. (1991). Free software helps map and display data. *Eos, Trans. AGU*, *72*(41), 441–446. https://doi.org/10.1029/90EO00319

Xu, M. J., and He, J. (2022). Seispy: Python module for batch calculation and postprocessing of receiver functions. *Seismol. Res. Lett.*, *94*(2A), 935–943. https://doi.org/10.1785/0220220288

Yang, F., Zhang, H., Li, J., Wang, X., and Chen, Q. F. (2021). Topography of mantle transition zone discontinuities beneath Northeast China imaged by receiver function with Ps scattering kernel. *Chinese J. Geophys.* (in Chinese), *64*(12), 4406–4424. https://doi.org/10.6038/cjg2021P0213

Ye, L. L., Li, J., Tseng, T. L., and Yao, Z. X. (2011). A stagnant slab in a water-bearing mantle transition zone beneath northeast China: implications from regional SH waveform modelling. *Geophys. J. Int.*, *186*(2), 706–710. https://doi.org/10.1111/j.1365-246x.2011.05063.x

Yoshino, T., Manthilake, G., Matsuzaki, T., and Katsura, T. (2008). Dry mantle transition zone inferred from the conductivity of wadsleyite and ringwoodite. *Nature*, *451*(7176), 326–329. https://doi.org/10.1038/nature06427

Zhang, H. Q., Egbert, G. D., and Huang, Q. H. (2022). A relatively dry mantle transition zone revealed by geomagnetic diurnal variations. *Sci. Adv.*, *8*(31), eabo3293. https://doi.org/10.1126/sciadv.abo3293

Zhang, M., Sun, D. Y., Wang, Y., and Wu, Z. Q. (2019). Fine structure of the 660-km discontinuity beneath southeastern China. *Geophys. Res. Lett.*, *46*(13), 7304–7314. https://doi.org/10.1029/2019GL082639

Zhao, D. P., Tian, Y., Lei, J. S., Liu, L., and Zheng, S. H. (2009). Seismic image and origin of the Changbai intraplate volcano in East Asia: Role of big mantle wedge above the stagnant Pacific slab. *Phys. Earth Planet. Inter.*, *173*(3-4), 197–206. https://doi.org/10.1016/j.pepi.2008.11.009

Zhou, B. X., and He, X. B. (2024). No basalt accumulation and segregation atop the 660-km discontinuity beneath the Sea of Okhotsk. *Earth Planet. Phys.*, *8*(4), 621–631. https://doi.org/10.26464/epp2024034

Zhu, S., Deng, Y. F., Xu, Y. G., Chen, Y., Zhang, Z., Li, H. Y., Li, Z. H., Wang, S. J., Wang, X., and Priestley, K. (2026). Heterogeneous stagnant slab controls focused crustal recycling and volcanic clustering. *Nat. Commun.*, *17*(1), 9835. https://doi.org/10.1038/s41467-026-76463-x